

Photoionization of Two Potential Biofuel Additives: γ -Valerolactone and Methyl Butyrate

Andrea Giustini,* Matthew Winfough, Joseph Czekner, Bálint Sztáray, Giovanni Meloni, and Andras Bodi*



Cite This: *J. Phys. Chem. A* 2021, 125, 10711–10724



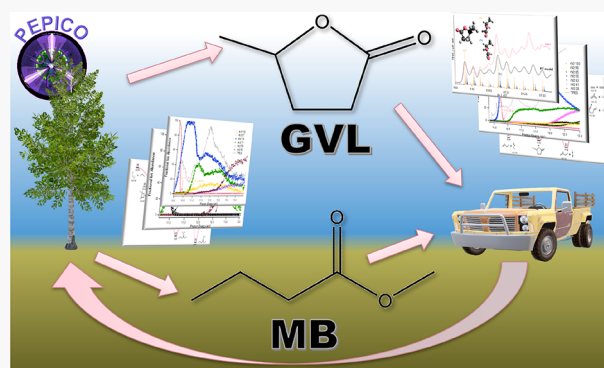
Read Online

ACCESS |

Metrics & More

Article Recommendations

ABSTRACT: The photoionization of two potential biofuel additives, γ -valerolactone (GVL, $C_5H_8O_2$) and methyl butyrate (MB, $C_5H_{10}O_2$) has been studied by imaging photoelectron photoion coincidence spectroscopy (iPEPICO) at the VUV beamline of the Swiss Light Source (SLS). The vibrational fine structure in the photoelectron spectrum is compared with a Franck–Condon simulation for the electronic ground-state band of the GVL cation. In the lowest energy dissociative photoionization channel of GVL, CO_2 is lost, resulting in a 1-butene fragment ion with a 0 K appearance energy of $E_0 = 10.35 \pm 0.01$ eV. A newly calculated 1-butene ionization energy of 9.595 ± 0.015 eV establishes the reverse barrier height to CO_2 loss as 66.6 ± 4.3 kJ mol $^{-1}$. Methyl butyrate cations undergo McLafferty rearrangement, which explains the missing ion signal at the computed adiabatic ionization energy of 9.25 eV. After H transfer, ethylene is lost in the lowest energy dissociation channel to yield the methyl acetate enol ion at $E_0 = 10.24 \pm 0.04$ eV. This value connects the energetics of methyl butyrate with that of methyl acetate enol ion, which is established at $\Delta H_{OK}^\circ[CH_2C(OH)OCH_3^+] = 502 \pm 6$ kJ mol $^{-1}$. Parallel to ethylene loss, methyl loss is also observed from the enol tautomer of the parent ion. Both samples exhibit low-energy nonstatistical dissociative ionization channels. In GVL, the methyl-loss abundance rises quickly but levels off suddenly in the energy range of the first electronically excited states, indicating nonstatistical competition between CH_3 and CO_2 loss. In MB, the major parallel dissociation channel is the loss of a methoxy radical. Calculations indicate that McLafferty rearrangement is inhibited on the excited-state surface. Indeed, breakdown curve modeling of this and a sequential CO -loss channel confirms a second statistical regime in dissociative photoionization, decoupled from ethylene loss.



1. INTRODUCTION

Dwindling fossil fuel supplies and pollution are major driving forces for finding cheap, clean, and renewable energy sources.¹ Biofuels derived from renewable materials are potentially attractive to replace fossil fuels.^{2,3} These biofuels include oxygenated species, such as alcohols,^{4–6} ethers,^{7,8} esters,^{2,9–11} and lactones.^{12–14} Accurate thermodynamic data are vital for kinetic modeling of combustion processes,¹⁵ and photoelectron spectroscopic fingerprints as well as the characterization dissociative photoionization (DPI) processes are invaluable to the isomer specific detection¹⁶ of precursors, reactive intermediates, and products in pyrolysis and combustion environments.^{17–20} In this study, we focus on two proposed fuel additives: γ -valerolactone (GVL, dihydro-5-methyl-2(3H)-furanone) and methyl butyrate (MB, methyl butanoate).

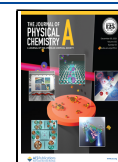
γ -Valerolactone has been proposed as a replacement to fuels and fuel blends because of its chemical properties and energy equivalency to petroleum based fuels.²¹ GVL is not prone to volatile emissions because of its high boiling point, 207 °C, and

low vapor pressure.¹³ It does not produce a measurable amount of peroxides after exposure to air at ambient conditions, either, and is unlikely to lead to violent explosions.¹⁴ GVL has a distinct smell, which makes it easy to detect spills or leaks and is also of interest as a low-toxicity, biodegradable green solvent.²² Czekner et al. have used photoionization mass spectrometry to measure the absolute photoionization cross section of biofuel candidates.²³ This experiment has also yielded a GVL ionization energy of 9.98 ± 0.05 eV, as well as appearance energies of DPI fragment ions corresponding to CO_2 and CH_3 loss, for which the authors also proposed tentative structures.

Received: September 11, 2021

Revised: December 6, 2021

Published: December 17, 2021



The production of esters as biofuel surrogates from vegetable oils and fatty acids through transesterification reactions has been studied extensively.^{9–11,24} MB has also shown promise of being generated from nonfood crops,^{25–28} thus allowing it to qualify as a second-generation biofuel. The photoionization of MB has been studied by photoelectron spectroscopy and photoionization mass spectrometry.^{29–32} Mazyar et al. have analyzed the ethene loss dissociative photoionization dynamics after parent ion isomerization by PEPICO³³ and provided a 0 K appearance energy, $E_0 = 10.275 \pm 0.010$ eV, to the enolic form of the methyl acetate cation at m/z 74, along with the associated microcanonical rate curve. In a more recent photoionization mass spectrometry (PIMS) study to determine absolute photoionization cross sections, Wang et al. have also proposed appearance energies of 10.90 ± 0.10 and 10.85 ± 0.10 eV for the m/z 71 and 87 daughter ions, respectively, along with an appearance energy of 10.15 ± 0.10 eV for the dominant m/z 74 fragment ion.³¹

This work fits into our broader efforts to apply PEPICO to study oxygen-containing organics with atmospheric or combustion chemistry relevance, with varying oxygen content and various functional groups. Here, we study the photoionization and the dissociative photoionization dynamics of GVL and MB using internal energy selection by imaging photoelectron photoion coincidence (iPEPICO) spectroscopy at the vacuum ultraviolet (VUV) beamline of the Swiss Light Source (SLS).^{34,35} GVL and MB are examined in the 9.8–13.0 and 10.0–14.0 eV photon energy range, respectively. Thanks to parent ion internal energy selection by monochromatic VUV single-photon ionization and photoelectron kinetic energy analysis, as well as the measurement of unimolecular dissociation rates in the $10^4 \text{ s}^{-1} < k(E) < 10^7 \text{ s}^{-1}$ range, we will be able to revisit the structure of CO_2 -loss product ion in GVL, formed over a sizable reverse barrier, and identify it as the 1-butene cation, instead of the methylcyclopropane structure proposed previously.²³ The breakdown diagram of MB is also analyzed in the statistical framework, which not only reveals sequential and parallel dissociation channels but also indicates that methoxy radical loss takes place in an excited electronic state, similar to OH loss in methanol³⁶ and 2-propanol.³⁷ In this excited state, γ -hydrogen transfer to the carbonyl group is kinetically inhibited.

As was shown in the rather complex case of adipic acid,³⁸ density functional theory and composite method calculations are nowadays capable of complementing and completing the reaction mechanism deduced from the breakdown diagram. In addition to confirming the transition-state energy leading to CO_2 loss in GVL cations and the isolated-state behavior of CH_3O loss in MB, we also confirm that methyl loss in MB cations takes place from the enol tautomer, formed by H-transfer after a McLafferty rearrangement.

2. EXPERIMENTAL SECTION

The iPEPICO apparatus located at the Paul Scherrer Institute (PSI) has been described in detail previously^{34,35} and only a summary will be provided here. Synchrotron radiation for the VUV beamline at the SLS is generated using a bending magnet;³⁵ it is collimated with a platinum-coated copper mirror and enters a turntable-style grazing incidence monochromator.³⁵ Only one of the three available silicon gratings (600 mm^{-1}) has been used in these experiments, which is best suited for high-resolution experiments between photon energies of 5 and 15 eV.³⁴ To suppress higher order

radiation, the dispersed light is collimated and directed into a differentially pumped gas filter³⁹ and filled over an optical length of 10 cm with 8–10 mbar of Ne, a 60% Ne, 30% Ar, and 10% Kr mixture, or a 75% Ne and 25% Ar mixture, depending on the photon energy.³⁹ The photon energy is calibrated using autoionization lines of argon in first and second order, confirming a photon energy resolution of around 3 meV at 10 eV.

Methyl butyrate (99%) and γ -valerolactone (98%) were purchased from Sigma–Aldrich. Samples were degassed and effused into the ionization region of the instrument through a 30 cm long, 6 mm outer diameter Teflon tube. A needle valve controlled the flow of sample vapor into the apparatus, held at a temperature of 298 K and a pressure between 1×10^{-6} and 3×10^{-6} mbar. Ions and electrons produced after VUV photoionization were accelerated using an extraction field of 120 and 125 V cm^{-1} , depending on whether the iPEPICO³⁴ or the iPEPICO capabilities of the CRF-PEPICO endstation were used.⁴⁰ Photoelectrons were velocity map imaged based on their off-axis momentum using a Roentdek DLD40 position sensitive delay line detector. This focused the zero kinetic energy electrons in a small center spot with better than 1 meV resolution at the threshold. Kinetic energy, “hot,” electrons without off-axis momentum constituted the hot electron background in the center spot, which was subtracted as proposed by Sztáray and Baer.⁴¹ Photoions were detected either on a nonimaging Chevron-stack of MCPs in the iPEPICO or by a Roentdek DLD40 delay line detection in the CRF-PEPICO setup after time-of-flight (TOF) analysis in a Wiley–McLaren-type first-order space focusing linear TOF mass spectrometer with the electron hit as TOF start signal.

The fractional abundance of parent and daughter ions are determined using the threshold photoionization TOF spectra at various photon energies and plotted in the breakdown diagram as a function of photon energy. The appearance of the breakdown diagram is characteristic of the dissociation mechanism, the sample temperature, and the internal energy distribution of the intermediate ions. Breakdown curves are also shifted to higher photon energies and broadened slightly by the kinetic shift associated with metastable parent ions.⁴²

Photoions are metastable above the dissociation threshold if their lifetime is commensurate with or larger than the characteristic time for mass analysis; i.e., some photoions with enough energy to dissociate are still detected as parent ions. Due to the long extraction region employing a low electric field, the cation residence time there is on the order of μs . Thus, the dissociation rate of metastable parent ions can be measured experimentally, by modeling the quasi-exponentially decaying asymmetric daughter ion TOF peak shapes if the dissociation rate (k) is between 10^4 and 10^7 s^{-1} .⁴³ Alternatively, the center of gravity of the daughter ion can be evaluated to a similar effect.⁴⁴ This sets apart iPEPICO measurements from most contemporary PIMS and coincidence experiments,^{45,46} because cation fragmentation rate curves can be directly measured, modeled, and extrapolated to the dissociative photoionization threshold. Thus, we can identify and model kinetic shifts quantitatively, notwithstanding the increased uncertainty of the extrapolated threshold energies. In fact, the resulting error bars may be an order of magnitude more than for first, fast dissociative ionization channels.^{47,48}

An ab initio Rice–Ramsperger–Kassel–Marcus (RRKM) statistical model is created to model kinetic shifts, based on computed harmonic vibrational frequencies and rotational constants of the neutral, the dissociating ions, and the transition states⁴³ and is used together with the instrument parameters to calculate a model breakdown diagram as well as predict the TOF spectra based on the dissociation rate constants.⁴⁷ The dissociation thresholds and, in the case of a slow dissociation or a competitive shift in parallel dissociations, the transitional frequencies are then fitted to reproduce the experimental data and obtain the experimental rate curves and 0 K appearance energies.

3. COMPUTATIONAL SECTION

3.1. Ab Initio Calculations. Quantum chemical calculations serve multiple purposes. First, computed harmonic vibrational frequencies and rotational constants are used to calculate the thermal energy distribution of the sample, the density of states of the parent ion, and the number of states of the transition states in the RRKM rate equation. We also rely on these state functions to compute the excess energy distribution among the neutral and ionic fragments and the newly created translational degrees of freedom in sequential dissociations. Density functional theory at the B3LYP/6-311++G(d,p) level is used to find the stationary points along the reaction coordinates and to calculate the vibrational frequencies at these geometries to confirm the nature of the stationary point as minimum or a saddle point (typically, a tight transition state). In dissociation reactions without a reverse barrier, the vibrational frequency analysis of the loose transition state has been carried out at an arbitrary geometry, in which the breaking bond is frozen at a bond length of 3–4 Å and the remaining internal coordinates are optimized.⁴⁹ These transition-state vibrational frequencies are then used in the first guess of the statistical model before the appearance energies and transitional frequencies are fitted to reproduce the experimental data. Second, these density functional calculations for the neutral sample and its cation can also be used to calculate the Franck–Condon factors and simulate the photoelectron spectrum in the double harmonic approximation using Gaussian 16.⁵⁰ Third, the geometry optimizations and scans reveal the parts of the potential energy surface that drive the ionic fragmentation processes. It is therefore desired to further refine the energetics of the stationary points using more accurate composite methods and ensure that the experimental model and the computed potential energy surface are indeed consistent with each other. The power of such a synergistic approach for characterizing the DPI dynamics is best illustrated by a recent study of dioxolane, in which six distinct DPI channels yield fragment ions at only three different masses, yet a consistent statistical model and reaction path calculations unambiguously determine the branching ratio of each channel as a function of photon energy.⁵¹ We therefore recalculated the stationary points, obtaining adiabatic ionization energies, IE, 0 K appearance energies, E_0 , and isomerization energies using the composite methods CBS-QB3, CBS-APNO, G4, and W1BD.⁵⁰ Although MB and, in particular, GVL are structurally similar to furfural, for which certain levels of theory yielded spurious minima in the cation,⁴² no such artifacts have been found herein.

3.2. Statistical Model. The breakdown curve of the fragment ion in a single, fast dissociation channel corresponds to the integral of the internal energy distribution of the parent

ion above the dissociation threshold. In threshold ionization, it can generally be assumed that this distribution corresponds to the thermal energy distribution of the neutral sample transposed into the ion manifold by the ionizing photon.

$$E_{\text{int}}^{\text{ion}} = h\nu + E_{\text{int}}^{\text{neutral}} - \text{IE} \quad (1)$$

where $E_{\text{int}}^{\text{ion}}$ is the internal energy of the parent ion, $h\nu$ is the photon energy, $E_{\text{int}}^{\text{neutral}}$ is the internal energy of the neutral molecule, and IE is the adiabatic ionization energy. Therefore, modeling the breakdown diagram only requires the thermal energy distribution of the neutral molecules in such simple cases.^{43,47}

Dissociation rates must be modeled explicitly if they are slow at threshold, leading to a kinetic shift, i.e., a blue shift and slight broadening of the breakdown diagram, or when two parallel channels result in a competitive shift, i.e., the belated onset of the higher onset channel in the breakdown diagram because its rate constant first has to rise to compete with the lower onset channel. In such cases, the dissociation rates are computed in the RRKM framework:

$$k(E) = \frac{\sigma N^{\ddagger}(E - E_0)}{h\rho(E)} \quad (2)$$

where σ is the reaction degeneracy, $N^{\ddagger}(E - E_0)$ is the sum of states in the transition state, h is Planck's constant, and $\rho(E)$ is the density of states of the fragmenting ion. Rigid activated complex RRKM theory (RAC-RRKM) has been proven flexible enough and accurate to describe metastable dissociations of small to medium sized ions with a tight transition state corresponding to a local maximum along the reaction potential energy curve. In the model, the frequencies of the vibrational modes that correspond to free translations and rotations in the products, also known as transitional modes, are scaled together to fit the model rate curve to the experimental data, and calculate the activation entropy, ΔS^{\ddagger} , which is typically negative for tight and positive for loose transition states.

The other model parameter to be varied is the dissociation threshold, i.e., the 0 K appearance energy of the daughter ion, E_0 . The uncertainty of the appearance energy around the optimized value is determined by scanning it while relaxing the other model parameters. The uncertainty limits correspond to the appearance energy values, at which the model cannot reproduce the experimental data acceptably anymore. In a dissociation along a purely attractive potential or if the local maximum energy lies below that of the fragment, the appearance energy corresponds to the dissociative photoionization energy. If the dissociation takes place along a bond breaking coordinate, the E_0 of the daughter ion yields the bond energy, BE, of the neutral if the fragment ion ionization energy is known:

$$\text{BE} = E_0 - \text{IE}_{\text{fragment}} \quad (3)$$

Furthermore, the appearance energy connects the enthalpies of formation of the neutral and the fragments in such cases and can often be used in thermochemical cycles to derive new energetics data, such as enthalpies of formation^{52,53} or proton affinities.⁵⁴ If there is a transition state at an energy higher than that of the products, the appearance energy can be used to determine the heat of formation of the activated complex accurately, which can be used, e.g., to benchmark computational approaches.⁵⁵

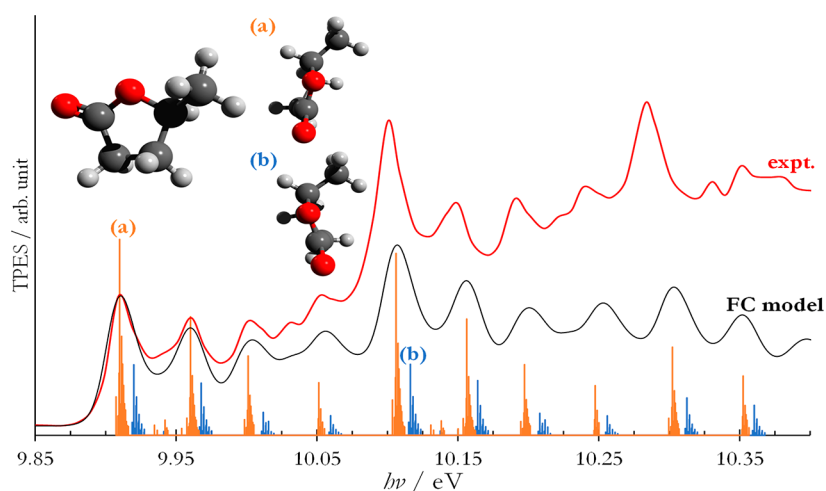


Figure 1. Ground-state GVL TPES shown together with the conformers (a) and (b) as well as a Franck–Condon simulation considering both conformers. The vibrational progressions are dominated by overtones and combination bands of ν_5 (O=C=O and CH₂–CH–CH₃ bend at 405 cm^{−1} in (a)) and ν_{11} (CH–O and CH₂–CO₂ stretch at 735 cm^{−1} in (a)). The vertical ionization energy at 10.11 eV corresponds to a singly excited overtone of ν_{31} (asymmetric O=C=O stretch at 1585 cm^{−1} in (a)). The FC line spectrum has been convoluted with a 20 meV full width at half-maximum Gaussian to account for the rotational envelope for comparison with the experimental spectrum.

4. RESULTS AND DISCUSSION

4.1. γ -Valerolactone. **4.1.1. Threshold Photoelectron Spectrum.** Figure 1 shows the GVL TPES in the 9.8–10.5 eV energy range together with a B3LYP/6-311++G(d,p) Franck–Condon simulation of the ground-state band. The simulation confirms the peak at 9.91 ± 0.01 eV to be the 0⁰ transition, which, after taking the Stark shift in a constant 120 V cm^{−1} into account,⁵⁶ yields an adiabatic ionization energy of $IE = 9.90 \pm 0.01$ eV. This value is only barely outside of the error bar of the previously reported ionization onset at 9.98 ± 0.05 eV.²³ As recently pointed out by Sánchez Valera et al. in a vibrational circular dichroism study,⁵⁷ GVL is chiral because of the environment of the γ -carbon. It also has two comparably stable conformers. The five-membered ring is not planar, and it may point away from or toward the methyl group in conformers (a) and (b), respectively, as shown in Figure 1. Conformer (a) is calculated to be 2.65 kJ mol^{−1} more stable than conformer (b) using the G4 composite method. The two are connected over a low-lying transition state of 7.3 kJ mol^{−1}, which implies thermal equilibrium, i.e., 74% (a) and 26% (b), at room temperature. The CBS-APNO calculated adiabatic ionization energies are 9.95 and 9.96 eV for conformers (a) and (b), respectively. Since they readily interconvert, both conformers may contribute to the photoelectron spectrum, and the Franck–Condon simulation of the two is obtained based on the experimental ionization energy and the calculated ionization energy difference and is weighted with their room-temperature abundance and by neglecting cross-conformer transitions. The GVL neutral density of states, thus, the thermal energy distribution of GVL in the statistical model, is based on the more stable (a) conformer. This rich conformational space is thanks to the five-membered ring and is lost in ionic fragmentation (see below).

We have also found a further cationic minimum at a CBS-QB3 calculated ionization energy of 10.44 eV in addition to the cation minima closest to the neutral conformers. This isomer has a shorter C=O bond length (1.15 vs 1.24 Å), a longer OC–O bond length (1.70 vs 1.27 Å), a shorter O–C(H)CH₃ bond length (1.34 vs 1.55 Å), and a longer C–CH₃ bond length (1.65 vs 1.50 Å) when compared with the GVL⁺

cation. In short, the bridging oxygen moves closer to the methyl carbon, and the methyl bond loosens in this isomer. In contrast to the furfural cation, in which similar isomer structures appear to be artifacts of the calculation, different density functional and wave function theory geometry optimizations agree about the existence of this isomer, even though it appears to sit in a very shallow (ca. 2 kJ mol^{−1}) potential energy well, which may not even support a bound vibrational state. Franck–Condon calculations predict no measurable intensity for transitions to this minimum; thus, it does not contribute to the photoelectron spectrum. However, it is the immediate precursor to the methyl-loss fragmentation product (see below).

Furthermore, and in contrast to the neutral, the enolic GVL tautomer is found to be more stable in the cation by 1.01 eV (CBS-QB3 computed $IE = 8.97$ eV) than the ketone. However, in contrast to MB (see below), there is no low-energy path to the enol, because vicinal H-transfer entails a barrier of 1.94 eV, owing to the steric strain in the transition state. Therefore, cation fragmentation easily outcompetes tautomerization, and the enol form of GVL is not expected to play a role in DPI. Both CO₂ and methyl losses are expected to take place from the ketone tautomer.

4.1.2. Breakdown Diagram. Threshold photoionization time-of-flight mass spectra are recorded for GVL over the 9.8–13.0 eV energy range, and the breakdown diagram is plotted in Figure 2a. From 9.8 to about 10.3 eV, the parent GVL ion is observed at m/z 100 in at a flight time of 18.87 μ s (Figure 2b). At about 10.0 eV, the TOF peak for the first fragment, m/z 56 by the loss of a 44 amu neutral, appears at 14.11 μ s in the mass spectrum and is slightly asymmetric at lower energies, indicating that its precursor, GVL⁺, is slightly metastable on the experimental time scale at low excess energies. The parent ion does not fully disappear from the TOF until about 10.35 eV. At approximately 10.50 eV, the second fragment, m/z 85, appears in the mass spectrum at a TOF of 17.40 μ s. Above approximately 11.80 eV, several channels open, with m/z 41 being the dominant one. One of the less intense channels, leading to m/z 43, appears at about the same energy. Above a photon energy of 12.48 eV, a new channel opens and yields $m/$

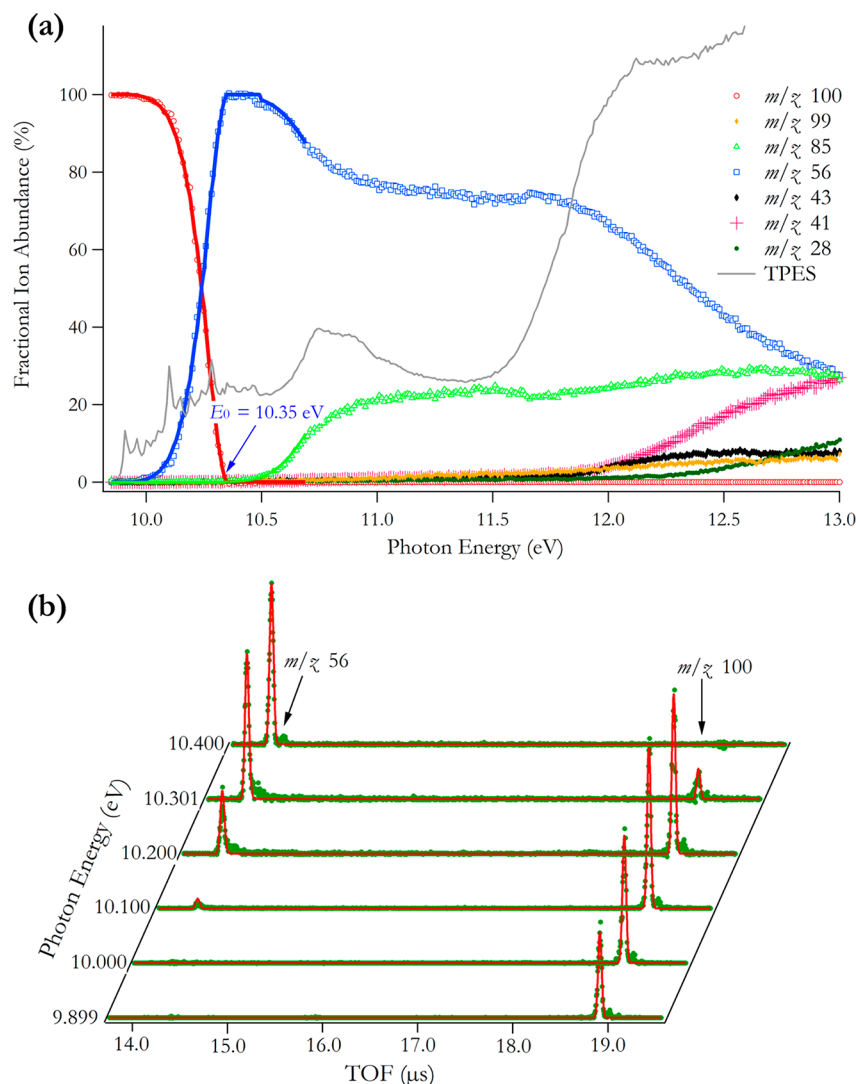


Figure 2. (a) Breakdown diagram of GVL in the 9.8–13.0 eV photon energy range. Red circles, blue squares, and green triangles are experimental points for m/z 100, 56, and 85, respectively, and solid lines represent the simulated breakdown diagram from the parent ion at m/z 100 to the 1-butene cation at m/z 56 by CO_2 loss and to m/z 85 by methyl loss. The gray line shows the threshold photoelectron spectrum (TPES) over the same energy range. (b) Time-of-flight distributions (dots) and fits (continuous lines) at six photon energies for the first dissociation step.

z 28. Finally, above a photon energy of 12.49 eV, m/z 99 appears.

Calculations lend support to chemical intuition and confirm the first, 44 amu loss channel below 10.5 eV yielding the m/z 56 fragment ion to be CO_2 loss. Carbon dioxide is an excellent leaving group, and its production in the analogous neutral systems has been investigated previously by both experiment^{58–60} and theory.⁶¹ Similar to CO_2 loss from the acetic acid anhydride cation,⁶² this process is expected to be exothermic in GVL^+ , as well. When the CO_2 moiety is removed from the cation core, DFT predicts a transition-state structure as shown in Figure 3a. Scanning along the intrinsic reaction coordinate confirms this to be the sole transition state between the GVL^+ cation and the 1-butene cation and carbon dioxide products. In the second step, when H transfer takes place to yield the 1-butene cation, only an inflection point is seen along the reaction energy curve while the leaving CO_2 is still near the ion.

As seen in the rate equation (eq 2), slow rates at threshold will result from a low transition-state number of states (tight transition state) or a large density of states (stable parent ion

with a deep potential energy well). Here, CO_2 loss is associated with a maximum energy transition state along the dissociation coordinate, but the parent GVL^+ ion is not strongly bound. The slight asymmetry in the daughter ion peaks has been modeled (Figure 2b), and the model indicates a small kinetic shift of less than 0.01 eV at an effective temperature of 280 K. The CBS-QB3 calculated transition-state energy, 10.43 eV (Figure 3b), is in reasonable agreement with the experimental $E_0 = 10.35 \pm 0.01$ eV. The enthalpy of formation of the activated complex can be obtained with the known enthalpy of formation of GVL, -406.5 ± 1.1 kJ mol⁻¹ at 298 K,⁶³ converted to -378.4 kJ mol⁻¹ at 0 K using the CBS-APNO thermal enthalpy, as $\Delta_f H_{0\text{K}}^\circ(\text{CO}_2\text{-loss TS}) = 620.2 \pm 4.0$ kJ mol⁻¹. The CO_2 and 1-butene 0 K enthalpies of formation are well-known at -393.1 ± 0.0 and 21.0 ± 0.4 kJ mol⁻¹, respectively,⁶⁴ whereas the 1-butene ionization energy is less well-defined at 9.55 ± 0.06 eV.⁶⁵ We compare accurately measured *cis*- and *trans*-2-butene ionization energies of 9.125 and 9.128 eV, respectively, by ZEKE spectroscopy by Ng et al.^{66,67} with CBS-APNO and WBD-computed ones. The CBS-APNO ones are in error by 0.046 and 0.049 eV, whereas

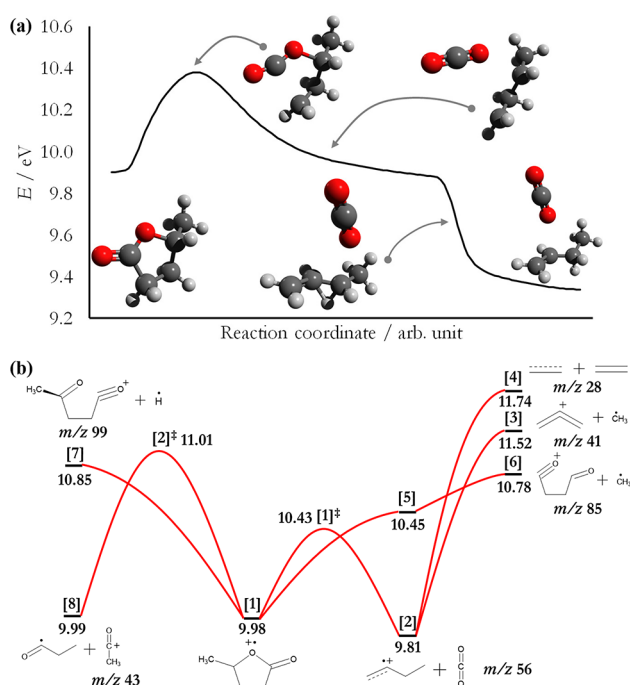


Figure 3. (a) DFT reaction path for CO_2 loss from the GVL cation relative to neutral GVL. CO_2 is removed first over a tight transition state corresponding to CO_2 becoming linear, followed by H transfer to form the 1-butene cation. The second step is only accompanied by an inflection point with CO_2 still loosely bound to the C_4 moiety. (b) CBS-QB3 potential energy surface of the GVL cation showing all the parallel dissociation channels. Energies are given relative to the neutral GVL in eV.

the W1BD IEs differ by 0.005 and 0.004 eV, respectively. Applying these discrepancies as corrections to the 1-butene calculations results yields a corrected CBS-APNO IE of 9.585 eV and a W1BD IE of 9.603 eV. Based on these results, we propose the ionization energy of 1-butene to be 9.595 ± 0.015 eV, which agrees perfectly with the early results of Dewar and Worley⁶⁸ and yields a 1-butene cation heat of formation of $\Delta H_{\text{OK}}^\circ[\text{C}_4\text{H}_8^+(\text{g})] = 946.7 \pm 1.6 \text{ kJ mol}^{-1}$. Based on the dissociative photoionization product energies and the enthalpy of formation of the activated complex, we can now calculate the reverse barrier height to be $66.6 \pm 4.3 \text{ kJ mol}^{-1}$.

In the 10.5–10.6 eV photon energy range, the methyl-loss fragment ion peak also appears in the breakdown diagram at m/z 85. Constrained geometry optimizations have confirmed that the methyl radical is lost along an almost purely attractive potential energy curve from an isomer cationic minimum with a shallow potential energy well 0.47 eV (CBS-QB3 value) above the most stable GVL^+ isomer, i.e., at 10.37 eV. In this isomer, the bridging oxygen in the ring moves from the $\text{C}=\text{O}$ group toward the CCH_3 carbon, after which the methyl group can be lost at CBS-QB3 and CBS-APNO computed dissociative photoionization energies of 10.78 and 10.76 eV, respectively. The rising edge of the methyl-loss breakdown curve can be reproduced quite well assuming a transition state with an activation entropy of $\Delta S_{600\text{K}}^\ddagger = 35 \text{ J (mol K)}^{-1}$, cf. the CO_2 -loss activation entropy of $\Delta S_{600\text{K}}^\ddagger = -9 \text{ J (mol K)}^{-1}$. While the loose transition state explains why methyl loss is competitive with CO_2 loss, the significantly larger methyl-loss rate constants also imply that it should swiftly become the dominant dissociative photoionization process as the internal energy is increased. This is not the case, as the methyl-loss

fractional abundance levels off at slightly over 20% and stays virtually constant over a 2 eV range. Thus, the partitioning of the reactive flux is not determined by the relative rates over a tight, low-energy and a loose, high-energy transition state. Isolated-state behavior, when a cation excited state is uncoupled from the ground state and dissociates differently, such as fluorine atom loss in tetrafluoroethylene cations,⁶⁹ is unlikely in GVL cations, because the absence of a Franck–Condon gap in the photoelectron spectrum implies that cation electronic states are closely spaced in energy. Furthermore, time-dependent DFT calculations at the B3LYP/6-311++G(d,p) level along the CO_2 and methyl-loss reaction coordinates in the GVL cation show reverse barriers in excess of 3 eV for both fragmentation processes in the excited electronic states. Thus, excited electronic cation states are stable with respect to fragmentation. We observe prompt fragment ion formation, which implies that relaxation to the ground electronic cation state is fast. How can the nonstatistical competition between CO_2 and methyl loss be explained under these circumstances? In fluorethene cations, statistical H, HF, and F atom losses are found to take place on the ground, \tilde{X}^+ state, whereas diabatic coupling onto the repulsive part of the \tilde{B}^+ -state surface are proposed to give rise to nonstatistical F loss.⁷⁰ Analogously, the coupling kinetics between the electronic ground and excited states and/or different reaction coordinates in the excited state may be responsible for the nonstatistical competition between these two channels and for preventing methyl loss from out-competing CO_2 loss in GVL^+ . Because of the size of the molecule and the number of internal degrees of freedom, a computational confirmation of this mechanism is not within our reach. Therefore, we only model the early competition between these two channels up to 10.7 eV (Figure 2a).

New dissociation channels open above 11.9 eV photon energy, the most dominant being m/z 41, likely the allyl cation. As the m/z 85 methyl-loss channel is barely affected by the rise of m/z 41, it is predominantly a sequential dissociation product of the CO_2 -loss fragment ion at m/z 56. The slowly rising slope of the allyl cation breakdown curve indicates large kinetic energy release (KER) in the CO_2 -loss step. This is due to impulsive dissociation after the system passes the high-energy transition state and its short lifetime thereafter, which precludes the statistical redistribution of the excess energy. The CBS-QB3 and CBS-APNO computed 0 K allyl cation appearance energy by sequential CO_2 and CH_3 loss is 11.52 and 11.55 eV, respectively. The methyl-loss onset of the dissociative ionization of 1-butene has been established as $11.36 \pm 0.06 \text{ eV}$,⁶⁵ i.e., 1.77 eV above the ionization energy of 1-butene. On the one hand, if we assume the excess energy below the CO_2 -loss transition state to be lost quantitatively in kinetic energy release, this implies a $1.77 + 10.35 = 12.12 \text{ eV}$ appearance energy for m/z 41. On the other hand, the assumption that a constant fraction of the total excess energy is lost to translations after a tight and energetic transition state reproduced the breakdown diagram of thymine quite well.⁷¹ Clearly, because of the nonstatistical competition between the primary CO_2 - and CH_3 -loss channels, the dynamic kinetic energy release in the former, and the possibility of 1-butene cation isomerization after its formation, the breakdown curve of the fast, sequential methyl-loss dissociation reaction is not reproducible by a simple statistical model.⁷² However, the experimental data still provide a snapshot of the m/z 56 internal energy distribution, as the fraction below and above

the sequential methyl-loss barrier is given by the m/z 56:41 ratio in the breakdown diagram. These snapshots can be used to validate a kinetic model of dissociative photoionization. However, only half of 1-butene loses methyl more than 1.5 eV above the thermochemical limit to allyl cation formation at 13 eV, which is why we do not attempt to characterize the KER distribution quantitatively.

Above a photon energy of 11 eV, a peak rises slowly at m/z 43 and levels off at constant abundance up to 13 eV. Because of the slowly changing fractional abundance, this channel corresponds to a parallel dissociation with the parent GVL⁺ cation as the only plausible precursor. The peak can be readily identified as protonated ketene, $\text{CH}_3\text{C}=\text{O}^+$, which is formed by H transfer to the methylene group in the five-membered ring, vicinal to the $\text{C}=\text{O}$ carbon. The neutral fragment at mass 57 amu is, thus, likely the 2-oxopropyl radical. The m/z 99 peak, corresponding to H loss from the parent ion exhibits a remarkably similar behavior to m/z 43, which supports the argument that the competitive mobilization of hydrogen atoms in the parent ion enables both channels in this energy range. For completeness, we mention that a minor peak appears at m/z 55 above a photon energy of approximately 11.9 eV and persists throughout the experimental energy range (not plotted in Figure 2a because its fractional abundance is always less than 5%). This can be attributed to a sequential H loss from 1-butene (m/z 56), at a CBS-QB3 calculated thermochemical limit of 11.28 eV. The m/z 56 fragment ion is also the precursor to the ethene cation at m/z 28 and rising above a photon energy of 12.3 eV. Although ethene cation and ethene formation from the 1-butene cation requires hydrogen atom migration, it is readily observed in the dissociative ionization of 1-butene, as well.⁶⁵

4.2. Methyl Butyrate. **4.2.1. Threshold Photoelectron Spectrum and Ionization Mechanism.** The ground-state TPES of MB consists of a single broad band (Figure 4a) due to an abundance of low-frequency vibrational modes, the rich configuration space of MB, and the, in part, large geometry change upon ionization. The ionization energy of MB has been studied several times^{29–32} and reported as 9.95 ± 0.05 eV in a previous PEPICO study,³³ whereas a calculated value of 9.977 eV has been given by Smialek et al.⁷³ However, the absence of a vibrational progression due to the large geometry change upon ionization makes it impossible to assign the origin transition with the help of a double harmonic Franck–Condon simulation of the ground-state band. Published ionization energies have often been found to be in error in such cases, for instance in ethanol or in diethyl ether,^{74,75} as the onset of the photoelectron spectrum only represents a likely upper limit to the adiabatic ionization energy. In an extreme case, adipic acid, the photoionization onset has been found to lie 1.5 eV above the adiabatic IE.³⁸ Thus, the MB photoelectron spectrum is of limited use to determine the ionization energy, and it is immaterial in this regard that our spectrum starts slightly above the ionization onset at 10 eV. Instead, we study the ionization of MB, in particular the role of conformational effects, using quantum chemical calculations. The exploration of the MB⁺ potential energy surface has also proven invaluable to understand the dissociative photoionization processes, as discussed in the next section.

Hernandez-Castillo et al.⁷⁶ have reported four low-energy methyl butyrate conformers as (a, a), (g_{\pm} , a), (a, g_{\pm}), and (g_{\pm} , g_{\pm}), all within less than 3 kJ mol^{−1} in energy (Figure 5). Based on the conformer energies and the barriers interconnect-

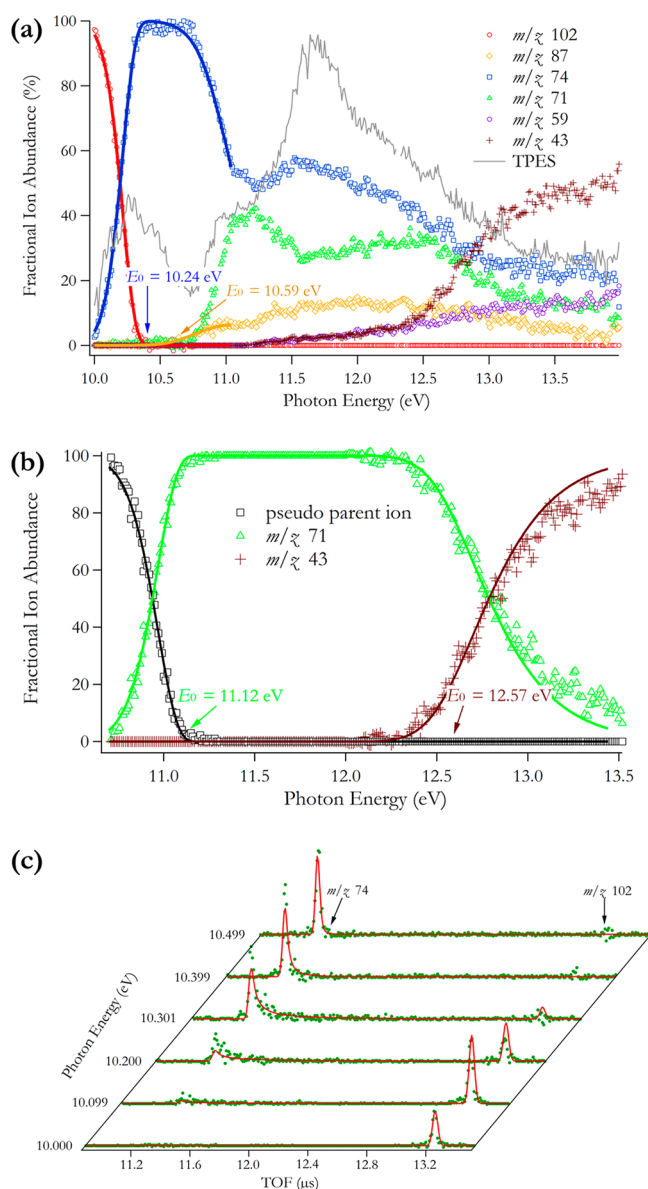


Figure 4. (a) Overview of the experimental breakdown diagram for MB over the 10.0–14.0 eV photon energy range. Solid lines represent the simulated breakdown diagram from the parent ion at m/z 102 in red to the methyl acetate enol cation at m/z 74 by ethene loss in blue and to the m/z 87 fragment ion in orange. The gray trace shows the threshold photoelectron spectrum (TPES) over the same energy range. (b) Breakdown diagram of the second statistical fragmentation regime showing the m/z 71 and sequential m/z 43 breakdown curves (see text). (c) Time-of-flight distributions (dots) and statistical fit (continuous lines) at six photon energies for the first, ethene-loss dissociation step.

ing them, (a, a) and (g_{\pm} , a) have been proposed to dominate the room temperature population. Figure 5 also lists the enol tautomer for completeness, in which a $\text{C}\alpha$ -hydrogen is transferred to the ketonic oxygen, and which is quite high in energy in the neutral but corresponds to the most stable ionic structure. Among the four MB conformers, (g_{\pm} , a) with the methyl group rotated toward the ketone group undergoes barrierless H-transfer upon vertical ionization; i.e., ionization is accompanied by major geometry change. Consequently, the Franck–Condon factors for this otherwise dominant neutral conformer cannot be evaluated easily and its contribution to

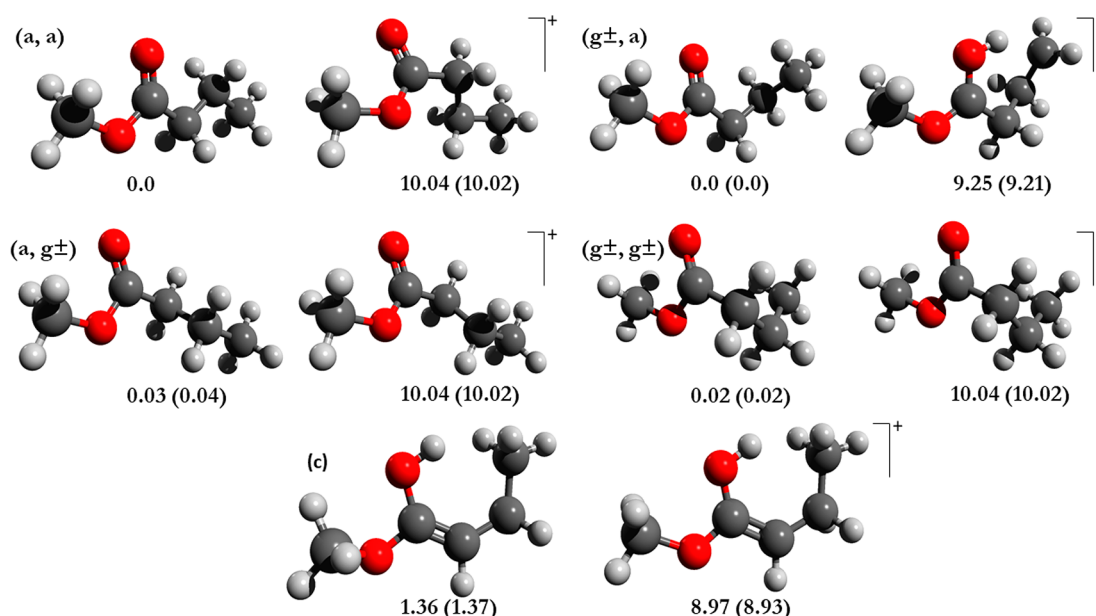


Figure 5. Structures of five neutral (left) and the corresponding cationic (right) structures of MB isomers shown together with CBS-QB3 and CBS-APNO (in parentheses) energetics given in eV. Values under each structure correspond to the energy with (a, a) as reference. The isoenergetic neutral minima (a, a) and (g±, a) correspond to very different cationic isomers, whereas the most stable enolic ion (c), is rather high in energy in the neutral.

the photoelectron spectrum remains elusive. Based on the MB ionization onset closely below 10 eV and the CBS-QB3-computed 9.25 eV (CBS-APNO: 9.21 eV) adiabatic and 10.51 eV vertical ionization energy of this isomer, the (g±, a) does not yield ion signal for at least 0.7 eV above its adiabatic ionization energy due to the large Franck–Condon gap, and its contribution at the onset of the ground-state photoelectron band is expected to be negligible. The remaining three MB conformers undergo more moderate geometry change and may play a significant role in photoionization at threshold, as they have a larger nuclear wave function overlap with the cation ground state.

While the photoionization signal is expected to be dominated by the abundant conformer (a, a), which does not undergo major geometry change upon ionization, the (g±, a) minimum can be reached from the (a, a), (a, g±), and (g±, g±) cationic structures by torsional motions over barriers no larger than a few kJ mol^{-1} . Thus, the low-energy (g±, a) cationic minimum determines the density of states of the parent MB^+ cation. We therefore use the CBS-QB3 computed adiabatic ionization energy to the (g±, a) cation from the (a, a) neutral of 9.25 eV to compute the parent ion density of states in the statistical model.

The enolic form of MB^+ is not easily accessible in the neutral, but similarly to GVL, it corresponds to the global minimum energy structure of the cation at a CBS-QB3 computed relative energy of 8.97 eV (CBS-APNO: 8.93 eV) to the ketone neutral, or an ionization energy of the enolic form of only 7.61 eV (CBS-APNO: 7.57 eV). Since its neutral population is negligible, it will not contribute to the photoelectron spectrum and is only mentioned here because of its role in dissociative photoionization processes via the cation conformer (g±, a) (vide infra).

As discussed above, at low energies, negligible Franck–Condon factors prevent the direct transition to cationic minimum (g±, a), although the corresponding neutral minimum is populated. At higher energies, the neutral

conformer (a, a), as well as the (a, g±) and (g±, g±) conformers ionize to the potential wells of the corresponding cationic minima, but these wells are connected by internal rotation to the cationic minimum (g±, a). Thus, ions with nonzero internal energy will undergo H-transfer. Time-dependent density functional theory (TD-DFT) at the B3LYP/6-311++G(d,p) level of theory, motivated by the appearance of the breakdown diagram, unveils a peculiar aspect of the electronic excited-state behavior of the MB cations. In the energy range of the first excited state, i.e., around 11 eV (see TPES in Figure 4), the neutral conformers will ionize to similar cationic geometries, but H transfer cannot take place, and the terminal CH_3 group will stay intact on the excited-state surface, which may allow the excited molecular ion to dissociate differently from the ground state. As will be discussed later, enol formation also becomes feasible in this energy range, at around 10.6–10.8 eV with respect to the neutral minimum.

4.2.2. Breakdown Diagram. Time-of-flight spectra are recorded in the 10.0–14.0 eV photon energy range. Between 10.0 and 10.3 eV, the parent ion of MB (m/z 102) is observed at a flight time of 13.25 μs with decreasing fractional abundance (Figure 4a,c). Above a photon energy of 10.1 eV, the TOF peak for m/z 74 ion appears and is found to be asymmetric at low energies, covering the 11.25–11.60 μs range. The parent ion disappears completely from the breakdown diagram at 10.4 eV photon energy, and two new peaks appear above 10.85 eV, at m/z 71 and 87. At yet higher energies, further two fragmentation channels open. The first one yields m/z 43 above a photon energy of ca. 11.5 eV. The final channel in the studied energy range yields the m/z 59 fragment ion, also above 11.5 eV.

The parent ion loses a 28 amu neutral fragment to form the m/z 74 ion in the lowest energy dissociation channel. As previously established, this corresponds to an ethylene loss yielding the 1-methoxyethen-1-ol cation.³³ Based on energetic and kinetic considerations, the alternative, CO loss, can be

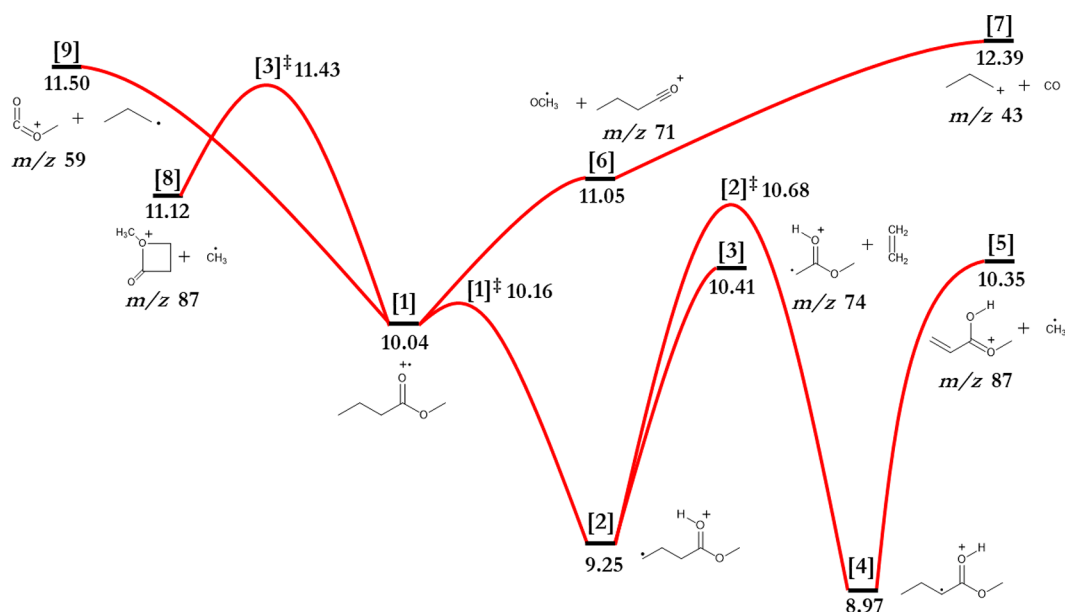


Figure 6. MB cation PES of all the primary dissociation channels. CBS-QB3 energies are relative to the MB conformer (a, a) neutral and are given in eV.

ruled out. At higher energies, parallel channels open by methyl and methoxy loss yielding m/z 87 and 71, as previously reported in a PIMS study by Wang et al.³¹ Again, based on reaction energetics, we can establish that the γ -methyl and the ester methoxy groups are lost, respectively. The rise of the major m/z 43 channel correlates with the decrease of the m/z 71 fragment ion, which establishes this channel as sequential 28 amu loss from the methoxy-loss intermediate. This step corresponds to CO loss yielding protonated propylene with a CBS-QB3 and CBS-APNO calculated thermochemical threshold of 12.39 and 12.35 eV, respectively.

The rise of the methyl-loss breakdown curve is slow, compatible with a slightly looser methyl-loss transition state yielding rates rivaling those of ethylene loss as the internal energy of parent ion increases. However, an analogous explanation fails to account for the methoxy-loss breakdown curve at m/z 71. The methoxy-loss signal rises steeply, which indicates an efficiently competing transition state looser than the ethylene-loss transition state. Yet, it stalls abruptly at less than 50% of the fractional abundance. Similar to methyl loss in GVL^+ , the branching ratio for this channel is, therefore, likely determined by factors that go beyond the relative statistical rate curves over the corresponding transition states, and methoxy loss competes with ethylene loss by a more complex mechanism. As discussed previously, γ -hydrogen transfer to the MB^+ ketone minimum is only possible on the ground electronic state. Consequently, if internal conversion to the electronic ground state is slower than intramolecular energy redistribution in the excited state, the molecular ion may be trapped in the excited state for a long enough time for it to dissociate.

Mazyar and Baer have explored the potential energy surface of the ground-state MB^+ cation at the MP2(full)/6-31G(d) level of theory and identified the low-lying distonic state, i.e., cation isomer ($g\pm$, a), with spatially separated radical and charge sites and the product of McLafferty rearrangement,^{77,78} as the precursor to C_2H_4 loss.³³ Our computed bond dissociation energies, as well as reverse barriers relative to the main photodissociation pathways are shown in the

potential energy surface of Figure 6, referenced to the CBS-QB3 calculated (a, a) neutral minimum. Instead of modeling the kinetics of the numerous isomerization steps, we assume that the parent ion density of states is determined predominantly by the distonic radical ion [2]. We located a transition state for the McLafferty rearrangement at 10.16 eV (CBS-QB3 value) and the distonic radical ion was found to be 9.25 eV above the ground neutral state. The ethylene-loss reaction path was obtained by scanning the $\text{C}_\beta\text{--C}_\gamma$ bond length of the conformers leading to a dissociation energy of 10.41 eV. All these values are calculated with respect to the most abundant isoenergetic (a, a) and ($g\pm$, a) conformers, and hereafter, for the sake of simplicity, we will refer to them when discussing the energetics of the upcoming channels. The transition-state number of states is determined based on its harmonic vibrational frequencies, and the transitional modes are fitted together with the E_0 to reproduce the breakdown diagram (Figure 4a) as well as the daughter ion time-of-flight distributions (Figure 4c) to account for the kinetic shift. The appearance energy of the best fit, $E_0 = 10.24 \pm 0.04$ eV, at an effective model temperature of 298 K, is slightly lower but in good agreement with the previously reported value of 10.275 ± 0.010 eV.³³

We will discuss the next statistical dissociation channel, parallel methyl loss from the parent ion. The dissociation barriers for direct methyl loss from cation isomers (a, a) and ($g\pm$, a) are above 11 eV, i.e., higher than the experimental observed threshold. Therefore, these channels can be ruled out. The ethylene moiety after methyl loss from the carbon chain in isomer (a, a) can also coordinate to the OCH_3 group to form a four-membered ring structure at a CBS-QB3 calculated energy of 10.78 eV, but this channel is associated with a prohibitively high-energy transition state at 11.43 eV. The methyl-loss channel opens up already at 10.35 eV from the enol tautomer of MB cation, which raises the question whether the enol isomer is accessible at such low energies. Indeed, H-transfer in the ionic isomer ($g\pm$, a) from the α -carbon to recreate the terminal methyl group and yield the enol tautomer may take place over a transition state at 10.68 eV (CBS-QB3

value), which leads us to propose that methyl loss takes place from the methyl butyrate enol tautomer. The fitted methyl-loss appearance energy of 10.59 eV, which we identify as the keto–enol transition-state energy, agrees well with the computed value and is significantly lower than the previously reported value of 10.85 eV.³¹

Methoxy loss, and the subsequent CO loss to yield m/z 71 and 43, respectively, appear to take place in an excited electronic state of the parent ion. This can be explained by faster dissociation compared with internal conversion to the ground electronic state, as well as the kinetically hindered H-transfer step in the McLafferty rearrangement on the excited-state potential energy surface. Thus, ions trapped in the excited electronic state of MB^+ may only decay by methoxy loss as they are stable with respect to alternative dissociation channels. The ground state of the methoxy radical is degenerate,⁷⁹ which is why both the \tilde{X}^+ and \tilde{A}^+ states of MB^+ correlate with the ground-state products, allowing us to calculate the appearance energies at the CBS composite methods. However, the m/z 43 signal starts to rise slowly slightly above 11.3 eV, after which it gains abundance much faster above 12 eV. The first, slow appearance of the m/z 43 signal may be due to a parallel process from the parent ion, in which a methyl radical and a CO_2 are lost sequentially. A straight line can be fitted to the m/z 43 fractional abundance 11.5–12.0 eV energy range to account for sequential $\text{CH}_3 + \text{CO}_2$ loss from the parent ion. The fractional abundance of m/z 71 above 10.7 eV in the second fragmentation regime can then be plotted relative to its maximum when it levels off in the region around 11 eV, 40%. The rest of the fragment ions is disregarded and only the sequential m/z 43 signal is considered additionally in the high-energy range of the breakdown diagram in Figure 4b. This breakdown diagram delivers a measure of the internal energy distribution of the intermediate $\text{CH}_3\text{CH}_2\text{CH}_2\text{CO}^+$, thanks to the sequential CO-loss channel following methoxy loss. In the absence of a kinetic shift, all species with sufficient internal energy will dissociate, and the breakdown diagram of the fragment ion corresponds to the integral of the internal energy distribution above the threshold. Similar to nonstatistical F loss in C_2F_4^+ ,⁶⁹ or the dissociative photoionization dynamics of carbon tetrachloride,⁸⁰ this allows us to establish whether this second dissociation regime is statistical within its phase space subspace. Thus, the statistical model shown in Figure 4b assumes fast methoxy loss from MB^+ followed by fast sequential CO loss together with a statistical redistribution of the excess energy. The fitted appearance energies arising from the modeling are found to be 11.12 and 12.59 eV for the first and the sequential dissociation channel, respectively. Considering the approximate excited-state breakdown diagram, these two values are in excellent agreement with the CBS-QB3 calculated appearance energies of 11.05 and 12.39 eV. The modeling clearly shows that this second dissociation regime generally behaves statistically besides it being decoupled from the McLafferty rearrangement in the electronic ground state, as only minor deviations from the statistical model are seen at high energies.

Finally, the last dissociation channel, corresponding to m/z 59 formation, can be ascribed to direct C–C cleavage at the parent ion α -carbon yielding CH_3CO_2^+ with a CBS-QB3 and CBS-APNO calculated thermochemical threshold of 11.50 and 11.46 eV, respectively.

4.2.3. Thermochemistry. The gas-phase thermochemistry of esters is less studied than that of other organics of similar size.

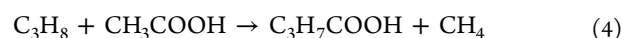
Ancillary thermochemical values and the results of this work are summarized in Table 1. A definitive value for the enthalpy

Table 1. Derived and Literature Values for Gas-Phase Enthalpies of Formation and Thermal Enthalpies Listed in kJ mol^{-1}

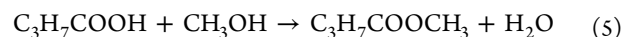
species	$\Delta_f H^\circ_{0\text{K}}$	$\Delta_f H^\circ_{298\text{K}}$	\pm	$H_{298\text{K}} - H_{0\text{K}}$	ref
γ -Valerolactone					
$\text{C}_5\text{H}_8\text{O}_2$	−378.4	−406.5 ^a	1.1	19.7 ^a	Leitao et al. ⁶³
Methyl Butyrate					
$\text{C}_3\text{H}_7\text{COOCH}_3$	−426	−458	8		Goos et al. ⁸³
	−425	−456	4	25.3	this work
Butyric Acid					
$\text{C}_3\text{H}_7\text{COOH}$	−430	−456	8		Goos et al. ⁸³
		−476	4		Chemistry Webbook ⁸⁴
		−473			Allinger et al. ⁸⁵
	−450	−476	4	21	this work
$\text{CH}_3\text{COOCH}_3$	−394.3	−413.2	0.6		ATcT ⁶⁴
CH_3COOH	−418.9	−433.0	0.4		
H_2O	−238.9	−285.8	0.0		
CH_3OH	−190.0	−200.9	0.2		
C_3H_8	−82.8	−105.0	0.2		
C_2H_4	60.9	52.4	0.1		
CH_4	−66.6	−74.5	0.1		
CO_2	−393.1	−393.5	0.0		
C_4H_8	21.0	0.1	0.4		
C_4H_8^+	946.7	926.5	1.6	17.8	this work
C				1.05	NIST-JANAF ⁸⁶
H				4.23	
O				4.35	

^aThermal enthalpy calculated herein.

of formation of acetic acid and methyl acetate is given in the Active Thermochemical Tables.^{64,81,82} The acetic and butyric acid enthalpies of formation are connected by the isodesmic reaction:



CBS-APNO yielded $\Delta_f H_{298\text{K}} = -12.6 \text{ kJ mol}^{-1}$ for the reaction enthalpy, which, together with the well-known 298 K enthalpies of formation of methane, propane, and acetic acid (Table 1) yields $\Delta_f H^\circ_{298\text{K}}[\text{C}_3\text{H}_7\text{COOH}(\text{g})] = -476 \pm 4 \text{ kJ mol}^{-1}$. This value is significantly lower than the $-456 \pm 8 \text{ kJ mol}^{-1}$ value given by Goos et al.⁸³ but agrees perfectly with the $-476 \pm 4 \text{ kJ mol}^{-1}$ value listed in the NIST Chemistry Webbook.⁸⁴ We can now check the methyl butyrate enthalpy of formation by calculating the reaction enthalpy of gas-phase esterification, which also happens to be an isodesmic reaction:



At the CBS-APNO level of theory, this yields a methyl butyrate enthalpy of formation of $\Delta_f H^\circ_{298\text{K}}[\text{C}_3\text{H}_7\text{COOCH}_3(\text{g})] = -456 \pm 4 \text{ kJ mol}^{-1}$, in near perfect agreement with the value listed by Goos et al.⁸³ The ethylene-loss appearance energy from MB, $10.24 \pm 0.04 \text{ eV} = 988 \pm 4 \text{ kJ mol}^{-1}$, connects the methyl butyrate with the methyl acetate enol ion. Using the 0 K heat of formation of ethene, $60.9 \pm 0.1 \text{ kJ mol}^{-1}$,⁶⁴ that of the methyl acetate enol cation is obtained at $502.1 \pm 6 \text{ kJ mol}^{-1}$. The computed reaction energy of methyl acetate yielding the methyl acetate

enol cation is 908.8 and 907.7 kJ mol⁻¹ using the CBS-APNO and W1BD composite methods, respectively, yielding $\Delta H^\circ_{\text{OK}}[\text{CH}_2\text{C}(\text{OH})\text{OCH}_3^+] = 513.9 \text{ kJ mol}^{-1}$, in good agreement with the dissociative photoionization value.

5. CONCLUSIONS

Imaging photoelectron photoion coincidence spectroscopy is used to measure the threshold photoelectron spectrum, breakdown diagram, and when applicable, dissociative photoionization rates of γ -valerolactone and methyl butyrate at the Swiss Light Source. Both samples have enol tautomers, which are less stable by more than 1 eV in the neutral, meaning that their population is negligible, and they will not contribute to the photoelectron spectrum. The ground-state photoelectron spectrum of the more rigid γ -valerolactone displays vibrational fine structure, which is due to vertical transition of the two low-energy conformers into the cation potential energy well. The enol tautomer is ca. 1 eV more stable than the ketone cation, but the rigid ring structure precludes a low-lying tautomerization mechanism, and the high barrier of vicinal H-transfer means the enol does not play a role in dissociative photoionization, either. The lowest lying dissociation channel of GVL⁺ is the exothermic CO₂ loss, which proceeds over a transition state and yields one 1-butene cation with a broadened internal energy distribution, due to suprathermal kinetic energy release. Based on the experimental appearance energy of $10.35 \pm 0.01 \text{ eV}$, a new, calculated 1-butene ionization energy of $9.595 \pm 0.015 \text{ eV}$, the reverse barrier height to CO₂ loss can be derived as $66.6 \pm 4.3 \text{ kJ mol}^{-1}$. The second, parallel methyl-loss dissociation channel shows a quickly rising and then plateauing behavior, which is inconsistent with a statistical process. We discuss possible reasons for the nonstatistical competition in the light of previously described nonstatistical halogen atom loss in dissociative ionization.

The ionization mechanism of methyl butyrate is discussed in the context of five neutral isomers and the corresponding ionic structures. The (a, a), (a, g \pm), and (g \pm , g \pm) conformers ionize without large geometry change and are proposed to dominate at least the low-energy TPES. An isoenergetic conformer (g \pm , a) with the methyl group pointing toward the carbonyl group undergoes H-transfer, i.e., McLafferty rearrangement upon ionization to the cationic ground electronic state. The adiabatic ionization energy of this conformer is calculated to be 9.25 eV (CBS-QB3 value), much lower than the ionization onset slightly below 10 eV. The large geometry change means that this conformer makes negligible contributions to photoionization at the threshold, but because of the easy interconversion with the other conformers on the cationic ground state, it drives the dissociative ionization kinetics and is responsible for ethylene loss as well as for the formation of the enol tautomer by further H-transfer. The ethylene-loss appearance energy of 10.24 eV, which corresponds to the dissociative photoionization energy to the methyl acetate enol cation and ethylene, is used to connect energetics of methyl acetate and methyl butyrate leading to a revision of the butyric acid enthalpy of formation to $-476 \pm 4 \text{ kJ mol}^{-1}$ and the methyl butyrate enthalpy of formation to $-456 \pm 4 \text{ kJ mol}^{-1}$. The enol tautomer ion is the methyl-loss precursor, which is a minor, parallel channel, subject to a competitive shift. Methoxy loss, another parallel channel, appears to compete very efficiently at first but then levels off below 50% fractional abundance, uncharacteristically for a statistical process. Indeed,

we find methoxy loss to be an isolated-state process on the excited state, in which the McLafferty rearrangement is kinetically prohibited. Due to slow internal conversion to the ground state, excited-state parent ions lose a methoxy group instead. By modeling the methoxy and the sequential CO losses using computed appearance energies, we can confirm this mechanism and that the second regime behaves statistically.

AUTHOR INFORMATION

Corresponding Authors

Andrea Giustini – Dipartimento di Scienze Fisiche e Chimiche, University of L'Aquila, 67100 L'Aquila, Italy; Email: andrea.giustini@graduate.univaq.it, giustiniandrea@gmail.com

Andras Bodi – Laboratory for Femtochemistry and Synchrotron Radiation, Paul Scherrer Institut (PSI), 5232 Villigen, Switzerland; orcid.org/0000-0003-2742-1051; Email: andras.boedi@psi.ch

Authors

Matthew Winfough – Department of Chemistry, University of San Francisco, San Francisco, California 94117-1080, United States

Joseph Czekner – Institut für Physikalische Chemie II, Karlsruhe Institute of Technology (KIT), 76131 Karlsruhe, Germany

Bálint Sztáray – Department of Chemistry, University of the Pacific, Stockton, California 95211, United States; orcid.org/0000-0002-0333-0000

Giovanni Meloni – Dipartimento di Scienze Fisiche e Chimiche, University of L'Aquila, 67100 L'Aquila, Italy; Department of Chemistry, University of San Francisco, San Francisco, California 94117-1080, United States; orcid.org/0000-0003-1697-5104

Complete contact information is available at: <https://pubs.acs.org/10.1021/acs.jpca.1c08033>

Notes

The authors declare no competing financial interest.

ACKNOWLEDGMENTS

The authors acknowledge the American Chemical Society – Petroleum Research Fund Grant # 51170 UNI6 and the University of San Francisco Faculty Development Fund. The authors also thank the Director of Scientific Computing, of the Department of Computer Science, Mr. A. Fedosov, at the University of San Francisco for providing for the space and general upkeep of the computer cluster used to perform the calculations. Additional computational support was provided by the Brown University Center for Computation and Visualization. In addition, J.C. thanks Dr. Zachary Piazza for providing scripts that aided in the data analysis and other helpful discussions. B.S. was supported by the National Science Foundation (Grant CHE-1665464). We gratefully acknowledge the Swiss Light Source for beamtime allocation.

REFERENCES

- (1) Chow, J.; Kopp, R. J.; Portney, P. R. Energy Resources and Global Development. *Science* **2003**, 302 (5650), 1528–1531.
- (2) Hoover, S. W.; Marner, W. D., 2nd; Brownson, A. K.; Lennen, R. M.; Wittkopp, T. M.; Yoshitani, J.; Zulkifly, S.; Graham, L. E.; Chaston, S. D.; McMahon, K. D.; et al. Bacterial production of free

fatty acids from freshwater macroalgal cellulose. *Appl. Microbiol. Biotechnol.* **2011**, 91 (2), 435–46.

(3) Ribeiro, B. D.; de Castro, A. M.; Coelho, M. A.; Freire, D. M. Production and use of lipases in bioenergy: a review from the feedstocks to biodiesel production. *Enzyme Res.* **2011**, 2011, 615803.

(4) Agarwal, A. K. Biofuels (alcohols and biodiesel) applications as fuels for internal combustion engines. *Prog. Energy Combust. Sci.* **2007**, 33 (3), 233–271.

(5) Atsumi, S.; Hanai, T.; Liao, J. C. Non-fermentative pathways for synthesis of branched-chain higher alcohols as biofuels. *Nature* **2008**, 451 (7174), 86–89.

(6) Rodriguez, G. M.; Atsumi, S. Synthetic Biology Approaches to Produce C3–C6 Alcohols from Microorganisms. *Curr. Chem. Biol.* **2012**, 6 (1), 32–41.

(7) Balakrishnan, M.; Sacia, E. R.; Bell, A. T. Etherification and reductive etherification of 5-(hydroxymethyl)furfural: 5-(alkoxymethyl)furfurals and 2,5-bis(alkoxymethyl)furans as potential bio-diesel candidates. *Green Chem.* **2012**, 14 (6), 1626.

(8) Frusteri, F.; Frusteri, L.; Cannilla, C.; Bonura, G. Catalytic Etherification of Glycerol to Produce Biofuels Over Novel Spherical Silica Supported Hyflon Catalyst. *Bioresour. Technol.* **2012**, 118 (August), 350–358.

(9) Otera, J. Transesterification. *Chem. Rev.* **1993**, 93 (4), 1449–1470.

(10) Park, E. Y.; Sato, M.; Kojima, S. Fatty acid methyl ester production using lipase-immobilizing silica particles with different particle sizes and different specific surface areas. *Enzyme Microb. Technol.* **2006**, 39 (4), 889–896.

(11) Schuchardt, U.; Sercheli, R.; Vargas, R. M. Transesterification of Vegetable Oils: A Review. *J. Braz. Chem. Soc.* **1998**, 9, 199–210.

(12) Mehdi, H.; Fábos, V.; Tuba, R.; Bodor, A.; Mika, L. T.; Horváth, I. T. Integration of Homogeneous and Heterogeneous Catalytic Processes for a Multi-step Conversion of Biomass: From Sucrose to Levulinic Acid, γ -Valerolactone, 1,4-Pentanediol, 2-Methyl-tetrahydrofuran, and Alkanes. *Top. Catal.* **2008**, 48 (1–4), 49–54.

(13) Horváth, I. T.; Mehdi, H.; Fábos, V.; Boda, L.; Mika, L. T. γ -Valerolactone - a Sustainable Liquid for Energy and Carbon-Based Chemicals. *Green Chem.* **2008**, 10, 238–242.

(14) Bond, J. Q.; Alonso, D. M.; Wang, D.; West, R. M.; Dumesic, J. A. Integrated Catalytic Conversion of γ -Valerolactone to Liquid Alkenes for Transportation Fuels. *Science* **2010**, 327, 1110–1114.

(15) Westbrook, C. K.; Dryer, F. L. Chemical kinetics and modeling of combustion processes. *Symp. Combust., [Proc.]* **1981**, 18 (1), 749–767.

(16) Bodi, A.; Hemberger, P.; Osborn, D. L.; Sztáray, B. Mass-Resolved Isomer-Selective Chemical Analysis with Imaging Photoelectron Photoion Coincidence Spectroscopy. *J. Phys. Chem. Lett.* **2013**, 4, 2948–2952.

(17) Bouwman, J.; Bodi, A.; Oomens, J.; Hemberger, P. On the formation of cyclopentadiene in the $C_3H_5^+ + C_2H_2$ reaction. *Phys. Chem. Chem. Phys.* **2015**, 17, 20508–20514.

(18) Savee, J. D.; Zádor, J.; Hemberger, P.; Sztáray, B.; Bodi, A.; Osborn, D. L. Threshold photoelectron spectrum of the benzyl radical. *Mol. Phys.* **2015**, 113, 2217–2227.

(19) Felsmann, D.; Moshhammer, K.; Krüger, J.; Lackner, A.; Brockhinke, A.; Kasper, T.; Bierkandt, T.; Akyildiz, E.; Hansen, N.; Lucassen, A.; et al. Electron ionization, photoionization, and photoelectron/photoion coincidence spectroscopy in mass-spectrometric investigations of a low-pressure ethylene/oxygen flame. *Proc. Combust. Inst.* **2015**, 35, 779–786.

(20) Hemberger, P.; Bodi, A.; Bierkandt, T.; Köhler, M.; Kaczmarek, D.; Kasper, T. Photoelectron Photoion Coincidence Spectroscopy Provides Mechanistic Insights in Fuel Synthesis and Conversion. *Energy Fuels* **2021**, 35 (20), 16265–16302.

(21) Vispute, T. P.; Huber, G. W. Breaking the Chemical and Engineering Barriers to Lignocellulosic Biofuels. *Int. Sugar J.* **2008**, 110, 138–149.

(22) Kerkel, F.; Markiewicz, M.; Stolte, S.; Müller, E.; Kunz, W. The green platform molecule gamma-valerolactone – ecotoxicity, biodegradability, solvent properties, and potential applications. *Green Chem.* **2021**, 23 (8), 2962–2976.

(23) Czekner, J.; Taatjes, C. A.; Osborn, D. L.; Meloni, G. Absolute photoionization cross-sections of selected furanic and lactonic potential biofuels. *Int. J. Mass Spectrom.* **2013**, 348, 39–46.

(24) Lepage, G.; Roy, C. C. Direct Transesterification of all Classes of Lipids in a One-step Reaction. *J. Lipid Res.* **1986**, 27, 114–120.

(25) Meher, L. C.; Sagar, D. V.; Nai, S. N. Technical aspects of biodiesel production by transesterification—a review. *Renewable Sustainable Energy Rev.* **2006**, 10 (3), 248–268.

(26) Tiwari, A. K.; Kumar, A.; Raheman, H. Biodiesel production from jatropha oil (*Jatropha curcas*) with high free fatty acids: An optimized process. *Biomass Bioenergy* **2007**, 31 (8), 569–575.

(27) Kromusa, S.; Wachter, B.; Koschuha, W.; Mandl, M.; Krotschecka, C.; Narodslawskyb, M. The Green Biorefinery Austria – Development of an Integrated System for Green Biomass Utilization. *Chem. Biochem. Eng. Q.* **2004**, 18 (1), 7–12.

(28) Mata, T. M.; Martins, A. A.; Caetano, N. S. Microalgae for biodiesel production and other applications: A review. *Renewable Sustainable Energy Rev.* **2010**, 14 (1), 217–232.

(29) Watanabe, K.; Nakayama, T.; Mottl, J. Ionization potentials of some molecules. *J. Quant. Spectrosc. Radiat. Transfer* **1962**, 2 (4), 369.

(30) Holmes, J. L.; Lossing, F. P. Gas-Phase Heats of Formation of Keto and Enol Ions of Carbonyl Compounds. *J. Am. Chem. Soc.* **1980**, 102 (5), 1591–1595.

(31) Wang, J.; Yang, B.; Cool, T. A.; Hansen, N. Absolute cross-sections for dissociative photoionization of some small esters. *Int. J. Mass Spectrom.* **2010**, 292 (1–3), 14–22.

(32) Howe, I.; Williams, D. H.; Kingston, D. G. I.; Tannenbaum, H. P. Substituent effects in the mass spectra of some γ - and β -substituted methyl butyrate. *J. Chem. Soc. B* **1969**, 4, 439–445.

(33) Mazzyar, O. A.; Baer, T. Ethene loss kinetics of methyl butanoate ions studied by threshold photoelectron–photoion coincidence: The enol ion of methyl acetate heat of formation. *Int. J. Mass Spectrom.* **1999**, 185–187, 165–177.

(34) Bodi, A.; Johnson, M.; Gerber, T.; Gengeliczki, Z.; Sztáray, B.; Baer, T. Imaging photoelectron photoion coincidence spectroscopy with velocity focusing electron optics. *Rev. Sci. Instrum.* **2009**, 80 (3), 034101.

(35) Bodi, A.; Hemberger, P.; Gerber, T.; Sztáray, B. A new double imaging velocity focusing coincidence experiment: i^2 PEPICO. *Rev. Sci. Instrum.* **2012**, 83 (8), 083105.

(36) Borkar, S.; Sztáray, B.; Bodi, A. Dissociative photoionization mechanism of methanol isotopologues (CH_3OH , CD_3OH , CH_3OD and CD_3OD) by i PEPICO: energetics, statistical and non-statistical kinetics and isotope effects. *Phys. Chem. Chem. Phys.* **2011**, 13 (28), 13009–20.

(37) Covert, K. J.; Bodi, A.; Torma, K. G.; Voronova, K.; Baer, T.; Sztáray, B. To roam or not to roam, that is the question for the methyl group in isopropanol cations. *Int. J. Mass Spectrom.* **2021**, 459, 116469–116469.

(38) Heringa, M. F.; Slowik, J. G.; Prévôt, A. S. H.; Baltensperger, U.; Hemberger, P.; Bodi, A. Dissociative Ionization Mechanism and Appearance Energies in Adipic Acid Revealed by Imaging Photoelectron Photoion Coincidence, Selective Deuteration, and Calculations. *J. Phys. Chem. A* **2016**, 120, 3397–3405.

(39) Johnson, M.; Bodi, A.; Schulz, L.; Gerber, T. Vacuum ultraviolet beamline at the Swiss Light Source for chemical dynamics studies. *Nucl. Instrum. Methods Phys. Res., Sect. A* **2009**, 610 (2), 597–603.

(40) Osborn, D. L.; Hayden, C. C.; Hemberger, P.; Bodi, A.; Voronova, K.; Sztáray, B. Breaking through the false coincidence barrier in electron-ion coincidence experiments. *J. Chem. Phys.* **2016**, 145, 164202.

(41) Sztáray, B.; Baer, T. Suppression of hot electrons in threshold photoelectron photoion coincidence spectroscopy using velocity focusing optics. *Rev. Sci. Instrum.* **2003**, 74, 3763–3768.

- (42) Winfough, M.; Voronova, K.; Muller, G.; Laguisma, G.; Sztaray, B.; Bodi, A.; Meloni, G. Furfural: The Unimolecular Dissociative Photoionization Mechanism of the Simplest Furanic Aldehyde. *J. Phys. Chem. A* **2017**, *121* (18), 3401–3410.
- (43) Baer, T.; Hase, W. L. *Unimolecular Reaction Dynamics Theory and Experiments*; Oxford University Press: New York, 1996.
- (44) West, B.; Joblin, C.; Blanchet, V.; Sztaray, B.; Mayer, P. M. On the Dissociation of the Naphthalene Radical Cations: New iPEPICO and Tandem Mass Spectrometry Results. *J. Phys. Chem. A* **2012**, *116*, 10999–11007.
- (45) Baer, T.; Tuckett, R. P. Advances in threshold photoelectron spectroscopy (TPES) and threshold photoelectron photoion coincidence (TPEPICO). *Phys. Chem. Chem. Phys.* **2017**, *19* (15), 9698–9723.
- (46) Wilson, K. R.; Qi, F. Probing Chemistry at Vacuum Ultraviolet Synchrotron Light Sources. In *Photoionization and Photo-Induced Processes in Mass Spectrometry*; Zimmermann, R.; Hanley, L., Eds.; Wiley-VCH: Weinheim, 2021; pp 159–213.
- (47) Sztaray, B.; Bodi, A.; Baer, T. Modeling unimolecular reactions in photoelectron photoion coincidence experiments. *J. Mass Spectrom.* **2010**, *45* (11), 1233–1245.
- (48) Stevens, W.; Sztaray, B.; Shuman, N.; Baer, T.; Troe, J. Specific rate constants $k(E)$ of the dissociation of the halobenzene ions: analysis by statistical unimolecular rate theories. *J. Phys. Chem. A* **2009**, *113* (3), 573–82.
- (49) Baer, T.; Sztaray, B.; Kercher, J. P.; Lago, A. F.; Bodi, A.; Skull, C.; Palathinkal, D. Threshold photoelectron photoion coincidence studies of parallel and sequential dissociation reactions. *Phys. Chem. Chem. Phys.* **2005**, *7*, 1507–1513.
- (50) Frisch, M. J.; Trucks, G. W.; Schlegel, H. B.; Scuseria, G. E.; Robb, M. A.; Cheeseman, J. R.; Scalmani, G.; Barone, V.; Petersson, G. A.; Nakatsuji, H.; et al. *Gaussian 16*, Rev. C.01; Gaussian Inc.: Wallingford, CT, 2016.
- (51) Weidner, P.; Voronova, K.; Bodi, A.; Sztaray, B. Dissociative photoionization of 1,3-dioxolane: We need six channels to fit the elephant. *J. Mass Spectrom.* **2020**, *55* (9), e4522.
- (52) Harvey, J.; Tuckett, R. P.; Bodi, A. A Halomethane Thermochemical Network from iPEPICO Experiments and Quantum Chemical Calculations. *J. Phys. Chem. A* **2012**, *116*, 9696–9705.
- (53) Matthiasson, K.; Kvaran, A.; Garcia, G. A.; Weidner, P.; Sztaray, B. Resolving the F2 bond energy discrepancy using coincidence ion pair production (cipp) spectroscopy. *Phys. Chem. Chem. Phys.* **2021**, *23* (14), 8292–8299.
- (54) Bodi, A.; Csontos, J.; Kállay, M.; Borkar, S.; Sztaray, B. On the protonation of water. *Chem. Sci.* **2014**, *5*, 3057–3063.
- (55) Rowland, T. G.; Borkar, S.; Bodi, A.; Sztaray, B. Iodine atom loss kinetics in internal energy selected 1-iodoalkane cations by imaging photoelectron photoion coincidence spectroscopy. *Int. J. Mass Spectrom.* **2015**, *378*, 134–142.
- (56) Chupka, W. A. Factors affecting lifetimes and resolution of Rydberg states observed in zero-kinetic-energy spectroscopy. *J. Chem. Phys.* **1993**, *98*, 4520–4530.
- (57) Sanchez Valera, M.; Casas Jaraices, R.; Montejo, M.; Rodriguez Ortega, P. G. Vibrational Circular Dichroism study of chiral food additives: gamma-valero- and gamma-caprolactone. *Spectrochim. Acta, Part A* **2021**, *247*, 119140.
- (58) James, T. L.; Wellington, C. A. Thermal Decomposition of β -Propiolactone in the Gas Phases. *J. Am. Chem. Soc.* **1969**, *91* (27), 7743–7746.
- (59) Frey, H. M.; Watts, H. P. Thermal Unimolecular Decomposition of B-Butyrolactone (4-Methyloxetan-2-one). *J. Chem. Soc., Faraday Trans. 1* **1983**, *79* (7), 1659–1668.
- (60) Frey, H. M.; Pidgeon, I. M. Thermal Decomposition of β -Propiolactone in the Gas Phase (Oxetan-2-one). *J. Chem. Soc., Faraday Trans. 1* **1985**, *81* (4), 1087.
- (61) Safont, V. S.; Andrés, J.; Domingo, L. R. A theoretical study on the decomposition mechanism of β -propiolactone and β -butyrolactone. *Chem. Phys. Lett.* **1998**, *288* (2), 261–269.
- (62) Voronova, K.; Mozaffari Easter, C. M.; Torma, K. G.; Bodi, A.; Hemberger, P.; Sztaray, B. Bifurcated dissociative photoionization mechanism of acetic acid anhydride revealed by imaging photoelectron photoion coincidence spectroscopy. *Phys. Chem. Chem. Phys.* **2016**, *18* (36), 25161–25168.
- (63) Leitao, M. L. P.; Pilcher, H.; Meng-Yan, Y.; Brown, J. M.; Conn, A. D. Enthalpies of combustion of γ -butyrolactone, γ -valerolactone, and δ -valerolactone. *J. Chem. Thermodyn.* **1990**, *22* (9), 885–891.
- (64) Ruscic, B.; Bross, D. H. Active Thermochemical Tables (ATcT) values based on ver. 1.122p of the Thermochemical Network <https://atct.anl.gov/> (accessed 2021-08-01).
- (65) van der Meij, C. E.; Van Eck, J.; Niehaus, A. The decomposition of $C_4H_8^+$ complexes at controlled internal energies. *Chem. Phys.* **1989**, *130*, 325–334.
- (66) Woo, H. K.; Zhan, J.; Lau, K.-C.; Ng, C. Y. Vacuum ultraviolet laser pulsed field ionization photoelectron study of cis-2-butene. *J. Chem. Phys.* **2002**, *116*, 8803–8808.
- (67) Woo, H. K.; Lau, K.-C.; Zhan, J.; Ng, C. Y. Vacuum ultraviolet laser pulsed field ionization photoelectron study of trans-2-butene. *J. Chem. Phys.* **2003**, *119*, 7789.
- (68) Dewar, M. J. S.; Worley, S. D. Photoelectron Spectra of Molecules. I. Ionization Potentials of Some Organic Molecules and Their Interpretation. *J. Chem. Phys.* **1969**, *50* (2), 654–667.
- (69) Harvey, J.; Bodi, A.; Tuckett, R. P.; Sztaray, B. Dissociation dynamics of fluorinated ethene cations: from time bombs on a molecular level to double-regime dissociators. *Phys. Chem. Chem. Phys.* **2012**, *14*, 3935–3848.
- (70) Harvey, J.; Hemberger, P.; Bodi, A.; Tuckett, R. P. Vibrational and electronic excitations in fluorinated ethene cations from the ground up. *J. Chem. Phys.* **2013**, *138* (12), 124301.
- (71) Majer, K.; Signorell, R.; Heringa, M. F.; Goldmann, M.; Hemberger, P.; Bodi, A. Valence Photoionization of Thymine: Ionization Energies, Vibrational Structure, and Fragmentation Pathways from the Slow to the Ultrafast. *Chem. - Eur. J.* **2019**, *25* (62), 14192–14204.
- (72) Sztaray, B.; Bodi, A.; Baer, T. Modeling unimolecular reactions in photoelectron photoion coincidence experiments. *J. Mass Spectrom.* **2010**, *45*, 1233–1245.
- (73) Śmialek, M. A.; Duflot, D.; Jones, N. C.; Hoffmann, S. V.; Zuin, L.; Macdonald, M.; Mason, N. J.; Limão-Vieira, P. On the electronic structure of methyl butyrate and methyl valerate. *Eur. Phys. J. D* **2020**, *74* (7), 153.
- (74) Bodi, A.; Brannock, M. D.; Sztaray, B.; Baer, T. Tunneling in H loss from energy selected ethanol ions. *Phys. Chem. Chem. Phys.* **2012**, *14*, 16047–16054.
- (75) Voronova, K.; Mozaffari Easter, C. M.; Covert, K. J.; Bodi, A.; Hemberger, P.; Sztaray, B. Dissociative Photoionization of Diethyl Ether. *J. Phys. Chem. A* **2015**, *119*, 10654–10663.
- (76) Hernandez-Castillo, A. O.; Abeysekera, C.; Hays, B. M.; Kleiner, I.; Nguyen, H. V. L.; Zwier, T. S. Conformational preferences and internal rotation of methyl butyrate by microwave spectroscopy. *J. Mol. Spectrosc.* **2017**, *337*, 51–58.
- (77) McLafferty, F. W. Mass Spectrometric Analysis. Molecular Rearrangements. *Anal. Chem.* **1959**, *31*, 82–87.
- (78) Gross, M. L. Focus in honor of Fred McLafferty, 2003 Distinguished Awardee, for the discovery of the “McLafferty Rearrangement. *J. Am. Soc. Mass Spectrom.* **2004**, *15*, 951–955.
- (79) Liu, J.; Chen, M.-W.; Melnik, D.; Yi, J. T.; Miller, T. A. The spectroscopic characterization of the methoxy radical. I. Rotationally resolved \tilde{A}^2A_1 – \tilde{X}^2E electronic spectra of CH_3O . *J. Chem. Phys.* **2009**, *130*, 074302.
- (80) Harvey, J.; Tuckett, R. P.; Bodi, A. Shining new light on the multifaceted dissociative photoionisation dynamics of CCl_4 . *Phys. Chem. Chem. Phys.* **2014**, *16*, 20492–20499.
- (81) Ruscic, B.; Pinzon, R. E.; Laszewski, G. v.; Kodeboyina, D.; Burcat, A.; Leahy, D.; Montoy, D.; Wagner, A. F. Active Thermochemical Tables: thermochemistry for the 21st century. *J. Phys.: Conf. Ser.* **2005**, *16*, S61–S70.

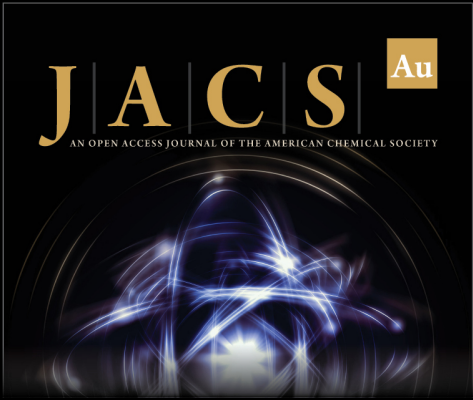
(82) Ruscic, B.; Pinzon, R. E.; Morton, M. L.; von Laszewski, G.; Bittner, S. J.; Nijssure, S. G.; Amin, K. A.; Minkoff, M.; Wagner, A. F. Introduction to Active Thermochemical Tables: Several “Key” Enthalpies of Formation Revisited†. *J. Phys. Chem. A* **2004**, *108* (45), 9979–9997.

(83) Goos, E.; Burcat, A.; Ruscic, B. Extended Third Millennium Ideal Gas and Condensed Phase Thermochemical Database for Combustion with updates from Active Thermochemical Tables. <http://burcat.technion.ac.il/dir/> (accessed 2021-08-01).


(84) Burtness, J. E. NIST Chemistry WebBook, NIST Standard Reference Database Number 69. <https://webbook.nist.gov/chemistry/> (accessed 2021-08-01).


(85) Allinger, N. L.; Schmitz, L. R.; Motoc, I.; Bender, C.; Labanowski, J. K. Heats of formation of organic molecules by Ab Initio calculations: Carboxylic acids and esters. *J. Comput. Chem.* **1992**, *13* (7), 838–841.


(86) Chase, M. W. NIST-JANAF Thermochemical Tables. <https://janaf.nist.gov/> DOI: DOI: 10.18434/T42S31 (accessed 2021-08-01).



JACS Au
AN OPEN ACCESS JOURNAL OF THE AMERICAN CHEMICAL SOCIETY

 Editor-in-Chief
Prof. Christopher W. Jones
Georgia Institute of Technology, USA

Open for Submissions 

pubs.acs.org/jacsau  **ACS Publications**
Most Trusted. Most Cited. Most Read.